OPTICS

Observation of photonic constant-intensity waves and induced transparency in tailored non-Hermitian lattices

Andrea Steinfurth[1], Ivor Krešić[2,3], Sebastian Weidemann[1], Mark Kremer[1], Konstantinos G. Makris[4,5], Matthias Heinrich[1], Stefan Rotter[2]*, Alexander Szameit[1]*

Light propagation is strongly affected by scattering due to imperfections in the complex medium. It has been recently theoretically predicted that a scattering-free transport through an inhomogeneous medium is achievable by non-Hermitian tailoring of the complex refractive index. Here, we implement photonic constant-intensity waves in an inhomogeneous, linear, discrete mesh lattice. By extending the existing theoretical framework, we experimentally show that a driven non-Hermitian tailoring allows us to control the propagation and diffraction of light even in highly disordered systems. In this vein, we demonstrate the transmission of shape-preserving beams and the seemingly undistorted propagation of light excitations across a strongly inhomogeneous non-Hermitian photonic lattice that can be realized by coupled optical fiber loops. Our results lead to a deeper understanding of non-Hermitian wave control and further contribute to the development of non-Hermitian photonics.

INTRODUCTION

Steering the flow of light by controlling the underlying propagation medium lies at the heart of photonics. The enormous impact of a medium's spatial structure and material properties on the light evolution is, on the one hand, a nuisance because undesired scattering, diffraction, or absorption can severely distort the propagation. On the other hand, faithfully tailoring the propagation medium allows one to fully control the light evolution such that the precise index engineering of media has become a popular research topic.

One established and well-investigated way of shaping the properties of a medium is called metamaterial (*1*). With the use of subwavelength structures, certain objects can be made invisible by cloaking them (*2*), or exotic parameters such as a negative refractive index can be achieved (*3*). In the past years, another methodology was developed to design an optical medium by using a complex refractive index involving gain and loss. Whereas losses have generally been considered an undesirable but inherent feature, the introduction of parity-time (PT) symmetry enhanced the richness of dynamics in non-Hermitian photonics by combining losses with gain (*4*). Faithfully controlling the spatial distribution of gain and loss led to many groundbreaking experiments that demonstrate a huge variety of fascinating properties, for example, branch points, spontaneous PT symmetry breaking and power oscillations (*4*–*6*), structures that exhibit exceptional points (*7*), optical solitons, and Bloch oscillations in PT-symmetric lattices (*8*, *9*) as well as PT symmetry breaking (*10*). Research in non-Hermitian photonics has lead, for example, to the invention of lasing media that act as a perfect absorber at the same time (*11*–*15*), lasing induced by loss (*16*, *17*), and topological lasers in photonic crystals (*18*, *19*). Attention was also attracted by the creation of potentials that are unidirectionally invisible and, in this context, enable reflectionless propagation or perfect transmission (*20*–*27*).

On the basis of the idea of fully controlling the complex refractive index distribution, the concept of constant-intensity waves has recently been introduced (*28*). This approach provides a systematic method to construct a complex medium such that an optical field can propagate through that medium with a desired intensity profile. Originally, this concept was put forward for infinitely extended waves, whose intensity was shown to remain constant all over space even in the presence of a highly nonuniform but appropriately engineered non-Hermitian dielectric design medium (*28*–*30*). Such constant-intensity waves do not necessarily require any nonlinear effects, as for solitons or solitary waves. Moreover, no underlying symmetries, like PT symmetry, are required to realize constant-intensity waves. Further studies of such tailored non-Hermitian potentials have transferred this idea also to discrete systems (*29*, *31*, *32*) or predicted pulsed light (*33*) as well as Gaussian-shaped beams (*34*, *35*) and showed that it is possible to construct finite wave packets that propagate in such inhomogeneous media with the same intensity distribution as in free space. Constant-intensity waves were also shown to have strong connections to the de Broglie-Bohm theory of quantum mechanics (*36*) and to the Jackiw-Rebbi modes of the Dirac equation (*37*). An experimental realization of these special waves has first been achieved in the field of acoustics in the form of constant-pressure sound waves (*38*). However, a photonic implementation of constant-intensity waves and their generalizations is still missing. Furthermore, an experimental verification of free-space beam diffraction in a disordered system (*34*, *35*) remains an entirely open problem, in particular in the field of non-Hermitian photonics.

In this work, we present the photonic realization of constant-intensity waves in a linear inhomogeneous discrete optical mesh lattice and extend this concept to the general tailoring of light diffraction in such systems. Our experiments are realized in coupled fiber loops (*9*, *39*), which have been used for experiments in many fields, ranging from Bloch oscillations (*40*) to optical solitons (*8*, *41*) and topological effects (*42*, *43*). Our results demonstrate that the

[1]Institute of Physics, University of Rostock, A.-Einstein-Str. 23, DE-18059 Rostock, Germany. [2]Institute for Theoretical Physics, Vienna University of Technology (TU Wien), A-1040 Vienna, Austria. [3]Institute of Physics, Zagreb 10000, Croatia. [4]ITCP-Physics Department, University of Crete, Heraklion 71003, Greece. [5]Institute of Electronic Structure and Lasers (IESL), Foundation for Research and Technology - Hellas, Heraklion 71110, Greece.
*Corresponding author. Email: alexander.szameit@uni-rostock.de (AS), stefan.rotter@tuwien.ac.at (SR)

non-Hermitian tailoring of a discrete propagation medium can be effectively used to realize optical constant-intensity waves in purely linear systems without PT symmetry and, more generally, to overcome the scattering induced by inhomogeneities.

RESULTS

As a starting point, we consider a beam that is launched into an inhomogeneous optical mesh lattice. Because of diffraction, scattering, and absorption in the medium, the output beam can develop strong intensity variations and will deviate considerably from its initial shape at the output (Fig. 1A). The crucial question that we address here is how the initial beam intensity can be maintained for any desired input beam. In linear Hermitian systems like perfectly straight waveguides or multimode fibers, such a feature could be naturally achieved by exciting a transverse eigenstate of the system. However, in non-Hermitian systems, the intensity of eigenstates is usually not conserved because of the nonvanishing imaginary part of the corresponding eigenvalue. Whereas in the presence of non-Hermitian symmetries, like unbroken PT symmetry, even non-Hermitian systems can exhibit a purely real eigenvalue spectrum, in inhomogeneous media without such symmetries, the spectra are in general complex. However, as recently predicted (*28*), it is possible to achieve propagation that preserves the constant intensity profile of an incoming wave even in non-Hermitian systems without PT symmetry, by tailoring the real and imaginary part of the potential of the propagation medium, i.e., its complex wave impedance. Here, we generalize this constant-intensity wave concept to the case of a Gaussian-shaped incoming beam with a spatially peaked intensity profile that propagates without any intensity distortions due to scattering or due to homogeneous lattice diffraction (Fig. 1B). In other words, the beam maintains both its Gaussian shape and its width throughout the entire propagation distance across the discrete tailored non-Hermitian lattice. Alternatively, an appropriate modification of the tailoring also allows us to suppress scattering while maintaining the homogeneous-lattice diffraction [see Fig. 1C and (*34*, *35*)]. The intensity distribution of a propagating single-site excitation in this case equals that of a perfectly homogeneous lattice, while the phase difference with respect to the homogeneous lattice propagation remains space dependent (see section S5). Our methodology for non-Hermitian tailoring is adapted to the respective input beam, which opens up the opportunity to realize an opaque lattice that becomes transparent for a certain spatial input distribution of amplitude and phase (see section S7). In the following, we will describe the underlying theoretical framework for such optical fiber loop lattices and experimentally implement both of the discussed cases in these photonic systems.

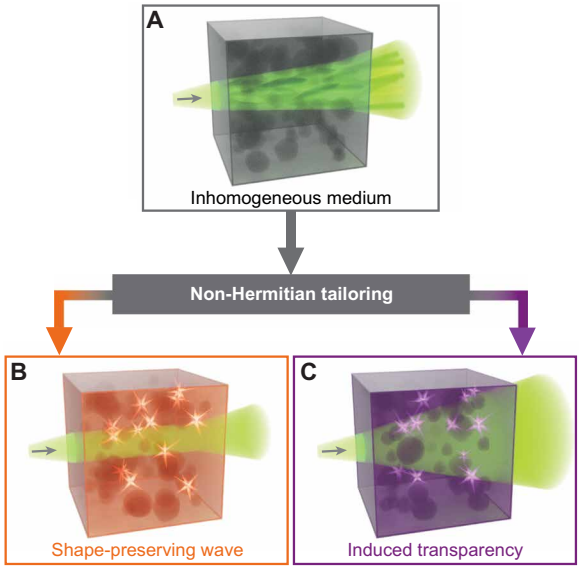

Fig. 1. Illustration of the concept: Shape-preserving waves and induced transparency in non-Hermitian tailored media. (**A**) A light wave propagating through a general inhomogeneous medium can acquire strong distortions of the initial intensity distribution due to undesired scattering or absorption. By tailoring the real and the imaginary part of the refractive index of the medium based on the input waveform, one can fully suppress the undesired distortions at will. This non-Hermitian tailoring can, for example, be applied to realize shape-preserving waves (**B**), in which the intensity profile of certain input beams remains unchanged along propagation inside the medium. The non-Hermitian tailoring can further be used to create any desired diffraction pattern, for instance, the diffraction inside a perfectly homogeneous medium, although the underlying medium is highly inhomogeneous (**C**). This induced transparency only occurs for a certain distribution of phase and amplitude of the input beam. In both cases (B) and (C), the tailoring can be adapted to any desired input beam.

Our experimental system consists of two optical fibers with slightly different length that are connected by a beam splitter (Fig. 2A; see Materials and Methods for experimental details). Light pulses propagating through this system perform a one-dimensional (1D) discrete-time quantum walk of a single quantum particle (*39*). The resulting dynamics of the corresponding wave function manifests in the pulse evolution in the fiber loops, which can be mapped onto the 1 + 1D photonic lattice (Fig. 2C) with time steps m and spatial positions n. The governing equations for the discrete amplitudes in the fibers are

$$\begin{aligned} u_n^{m+1} &= \frac{1}{\sqrt{2}}(u_{n+1}^m + iv_{n+1}^m)\, G_n^m\, e^{i\varphi_n^m} \\ v_n^{m+1} &= \frac{1}{\sqrt{2}}(v_{n-1}^m + iu_{n-1}^m)\, F_n^m\, e^{i\psi_n^m} \end{aligned} \tag{1}$$

where u_n^m and v_n^m are the left and right traveling complex amplitudes in the lattice at time step m and position step n, respectively. Amplitude modulators allow us to introduce controlled gain-loss modulations F_n^m, G_n^m of the lattice, i.e., the imaginary part of the underlying lattice potential for amplitude modulation. Additional phase modulators (PMs) are used to induce phase shifts φ_n^m, ψ_n^m representing the real part of the lattice potential. Both modulations allow us to fully control the complex wave impedance of the emulated discrete medium that, for instance, can correspond to its complex refractive index. A single-site excitation

$$\begin{aligned} u_n^0 &= 0 \\ v_n^0 &= \delta_{n0} \end{aligned} \tag{2}$$

of the homogeneous lattice with parameters $F_n^m = G_n^m = 1$ and $\varphi_n^m = \psi_n^m = 0$ results in the characteristic discrete diffraction pattern of the 1D discrete-time quantum walk (Fig. 2B).

Shape-preserving beam transmission

In our first set of experiments, we derive static lattice parameters that lead to a shape-preserving propagation for a desired input beam that we then implement experimentally. To this end, we use

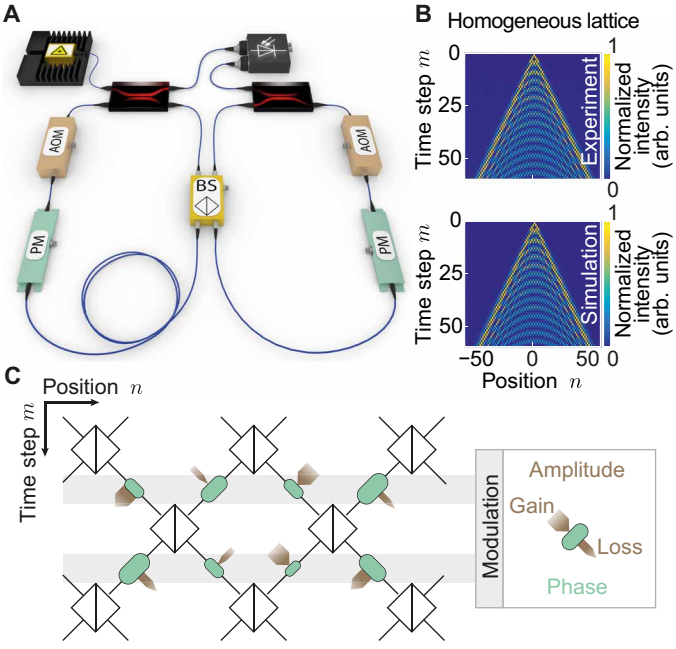

Fig. 2. Experimental implementation of non-Hermitian tailored photonic lattices. (**A**) The simplified experimental setup consists of two unequally long optical fiber loops, which are connected by a 50/50 beam splitter (BS). In each loop, an acousto-optic modulator (AOM) can modulate the amplitude of the propagating light and therefore emulate gain/loss modulations F_n^m, G_n^m in the lattice, corresponding to the imaginary part of the refractive index. In a similar way, a phase modulator (PM) in each loop controls the real part of the lattice potential via φ_n^m, ψ_n^m, corresponding to the real part of the refractive index. (**B**) Upon injecting a laser pulse into the loops, the developing pulse dynamics, detected by photodiodes, can be mapped onto a 1 + 1D discrete lattice, as is shown, for example, for the homogeneous case $F_n^m, G_n^m = 1$ and $\varphi_n^m, \psi_n^m = 0$ based on Eq. 1. The depicted intensities are the pulse intensities in the shorter loop. The evolution shows a discrete diffraction pattern, known from discrete-time quantum walks (*39*). (**C**) A part of the emulated mesh lattice is shown. The propagation in the fiber loops maps onto a mesh lattice of beam splitters and modulators (see the "Implementation of a 1 + 1D time bin–encoded optical mesh lattice" section in Materials and Methods for details), which are here depicted as capsules.

the straightforward ansatz of a time-independent amplitude and phase distribution in each loop

$$u_n^m = A_n e^{i\xi_n} \qquad v_n^m = B_n e^{i\eta_n} \tag{3}$$

with the amplitudes A_n, B_n that can be chosen freely to fit any desired intensity distribution of an input beam. As we aim to control merely the wave's intensity, there are no restrictions for the spatial phase distributions ξ_n, η_n, which remain as additional degrees of freedom. As a general example, we have chosen a Gaussian input beam

$$A_n = B_n = e^{-\frac{(n-n_0)^2}{2\sigma^2}} \tag{4}$$

with center position n_0 and width σ, as this is a very common pulse profile, which has also been theoretically considered in related works (*32*, *34*, *35*). By inserting the ansatz of Eq. 3 with the Gaussian amplitude distribution of Eq. 4 into Eq. 1, we derive the distribution for the parameters of the lattice with the initial phase distributions ξ_n, η_n as additional degrees of freedom. The derivation is given in details in section S1. The resulting solution for the lattice parameters reads

$$\begin{aligned}
\tan(\varphi_n) &= \frac{\sin(\xi_{n+1}-\xi_n)+\cos(\eta_{n+1}-\xi_n)}{\sin(\eta_{n+1}-\xi_n)-\cos(\xi_{n+1}-\xi_n)} \\
\tan(\psi_n) &= \frac{\cos(\xi_{n-1}-\eta_n)+\sin(\eta_{n-1}-\eta_n)}{\sin(\xi_{n-1}-\eta_n)-\cos(\eta_{n-1}-\eta_n)} \\
G_n &= \frac{\sqrt{2}\, e^{\frac{2(n-n_0)+1}{2\sigma^2}}}{\cos(\xi_{n+1}+\varphi_n-\xi_n)-\sin(\eta_{n+1}+\varphi_n-\xi_n)} \\
F_n &= \frac{\sqrt{2}\, e^{\frac{1-2(n-n_0)}{2\sigma^2}}}{\cos(\eta_{n-1}+\psi_n-\eta_n)-\sin(\xi_{n-1}+\psi_n-\eta_n)}
\end{aligned} \tag{5}$$

In a next step, we experimentally implement the non-Hermitian tailored lattice described by Eq. 5 for a Gaussian excitation with a width of σ = 30 and center $n_0 = 0$. Details on the generation of the Gaussian amplitude distribution are provided in the Supplementary Materials. To further benchmark the model and verify its universality, we choose the phase distribution for the initial Gaussian to be randomly perturbed along space. In Fig. 3, we compare the experimental propagation of a Gaussian-shaped beam in the appropriately tailored lattice (Fig. 3A) to the evolution of the beam upon exciting a general inhomogeneous lattice that does not satisfy Eq. 5, shown in Fig. 3B. Without a suitable tailoring, one can clearly see that the Gaussian shape is severely distorted after only a few time steps. In contrast, in the tailored non-Hermitian lattice, both the Gaussian shape and the beam width are well preserved for a much higher number of time steps. In Fig. 3B, there is a noticeable branching of the light flow (*44*). The duration from $m = 0$ to the appearance of the first "cusp" is approximately 10 time steps, while in the tailored non-Hermitian lattice the Gaussian propagates unmodulated for several times this distance. Moreover, we choose both lattices of Fig. 3 such that the only difference between their lattice parameters is the gain/loss modulation of Eq. 5, as the gain/loss modulation is added only in the non-Hermitian tailored system. Therefore, our results further show that a suitable distribution of the imaginary part of the refractive index can completely compensate the scattering effects that are induced by the real part of the refractive index. Note that the weak intensity variations in the tailored system are a result of the limited experimental accuracy with which we can match the Gaussian input shape as well as the lattice parameters. For ideally matched parameters, one also observes an ideal shape-preserving beam propagation (as demonstrated in section S2). In our experimental setup, the modulators are electrically controlled and the relation between applied voltage and actual modulation has been benchmarked in the setup. We estimate the error between the desired and applied modulation to be less than 4%. In addition, because of fluctuations and environmental influences on the experiment, also the initial intensity distribution is slightly perturbed. These errors slowly accumulate during ongoing propagation. Although the tailoring of shape-preserving beam transmission requires a high accuracy, we could obtain a clear Gaussian beam shape for an extended propagation length.

Non-Hermitian–induced transparency

In a second set of experiments, we explore how an appropriate dynamic tailoring that changes in time allows the implementation of any desired evolution pattern of the beam—an effect that was theoretically suggested only recently (*34*).

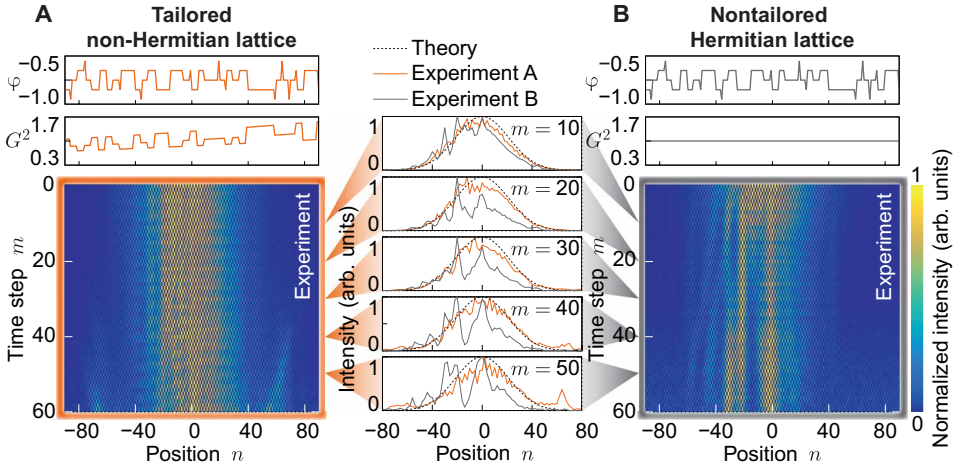

Fig. 3. Photonic realization of shape-preserving constant-intensity waves. The experimental propagation data in the tailored lattice are compared to a general inhomogeneous lattice, upon injecting a Gaussian beam at time step $m = 0$. The initial phase of the Gaussian has additionally been perturbed to show the versatility of the model. (**A**) When the real and imaginary part of the complex wave impedance of the lattice is tailored to fulfill the solution (Eq. 5), the Gaussian shape remains undistorted for a large number of time steps, yielding a shape-preserving beam solution. (**B**) In the case without a suitable complex tailoring, the initial Gaussian shape is quickly distorted after only a few time steps. Note that the underlying potential is static (meaning uniform and not driven at every time step). The normalized intensities (to the maximum value of each time step) in the shorter loop $|u_n^m|^2$ are depicted. To simplify the visualization, only the phase and gain/loss modulations of the *u* loop are shown. The full modulation pattern and the exact input phase of the input beam are described in detail in section S2.

In our experiments, we pick as an example a non-Hermitian modulation that completely suppresses the impact of scattering and restores diffraction of a single-pulse initial excitation that would occur in a homogeneous optical mesh lattice. As a result, the tailored lattice becomes fully transparent for the desired input beam with a specific phase and amplitude distribution (Fig. 2B), while the lattice would be highly opaque for other beams (see section S7). To derive the required modulation of the non-Hermitian potential, we modify the previous propagation condition given by Eq. 3 by introducing the desired time-dependent amplitude distributions I_n^m, J_n^m. To test the versatility of this extended model, we choose the time-independent phase distributions ξ_n, η_n that contain random perturbations along the position n. The corresponding approach reads

$$\begin{aligned} u_n^m &= iI_n^m e^{i\xi_n} \\ v_n^m &= J_n^m e^{i\eta_n} \end{aligned} \tag{6}$$

To emulate the transmission of a discrete propagation pattern in homogeneous lattices, as shown in Fig. 2B, we use the same single-site excitation of Eq. 2. The amplitudes I_n^m, J_n^m of the discrete diffraction pattern that develop upon the single-site excitation of the homogeneous lattice can be derived analytically (see sections S4 and S5), and this solution is then used in Eq. 6 to determine the lattice tailoring, which then reads

$$\begin{aligned} \tan(\varphi_n^m) &= \frac{I_{n+1}^m \sin(\xi_n - \xi_{n+1}) + J_{n+1}^m \sin(\xi_n - \eta_{n+1})}{I_{n+1}^m \cos(\xi_{n+1} - \xi_n) + J_{n+1}^m \cos(\eta_{n+1} - \xi_n)} \\ \tan(\psi_n^m) &= \frac{I_{n-1}^m \sin(\xi_{n-1} - \eta_n) - J_{n-1}^m \sin(\eta_{n-1} - \eta_n)}{J_{n-1}^m \cos(\eta_{n-1} - \eta_n) - I_{n-1}^m \cos(\xi_{n-1} - \eta_n)} \\ G_n^m &= \frac{\sqrt{2}\, I_n^{m+1}}{I_{n+1}^m \cos(\xi_{n+1} + \varphi_n^m - \xi_n) + J_{n+1}^m \cos(\eta_{n+1} + \varphi_n^m - \xi_n)} \\ F_n^m &= \frac{\sqrt{2}\, J_n^{m+1}}{J_{n-1}^m \cos(\eta_{n-1} + \psi_n^m - \eta_n) - I_{n-1}^m \cos(\xi_{n-1} + \psi_n^m - \eta_n)} \end{aligned} \tag{7}$$

In the same fashion as before, we also compare for this experiment the fully tailored non-Hermitian potential with a lattice that lacks the gain/loss modulation and, therefore, only satisfies the first two equation of Eq. 7. The resulting propagation of a single-site excitation is illustrated in Fig. 4. The fully tailored non-Hermitian system successfully shows a high similarity to the discrete diffraction pattern of Fig. 2B even up to a high number of propagation steps (see Fig. 4A). In the absence of the non-Hermitian modulation, the single-site excitation is scattered at the inhomogeneous lattice potential (see Fig. 4B). Again, the limited experimental accuracy of the lattice parameters leads to residual deviations in the intensity, which can be quantified by the normalized sum of squared differences (SSD)

$$\mathrm{SSD} = \sum_{n,m} \left(|u_n^{m,\mathrm{exp}}|^2 - |u_n^{m,\mathrm{sim}}|^2\right)^2 \Big/ \left(2\sqrt{\sum_{n,m} (|u_n^{m,\mathrm{exp}}|^2\, |u_n^{m,\mathrm{sim}}|^2)^2}\right) \tag{8}$$

where the sum covers the space displayed in the figures. The SSD quantifies the discrepancy of the experimentally measured intensity distributions in Fig. 4 (A and B) ("exp") from the simulated ideal unscattered Hermitian case ("sim"; see also Fig. 2B) ranging from 0 (best case) to 1 (worst case). For the calculation of the SSD, the data have been prepared according to the "Calculation of the deviations between experiment and simulation for induced transparency" section in Materials and Methods, which includes normalization to the sum of each time step. The SSD for the tailored non-Hermitian case has the value of 0.133, while, for the Hermitian case, it is 0.246. The difference from the optimal value of 0 in the non-Hermitian case is a consequence of the above-stated experimental imperfections. For a better comparison, we have also calculated the SSD for random intensity distributions taking only lattice sites into account that can actually be reached after the single-site excitation of the simulated propagation (same sublattice), which leads to an average of 0.313. For more details, see the "Calculation of the deviations

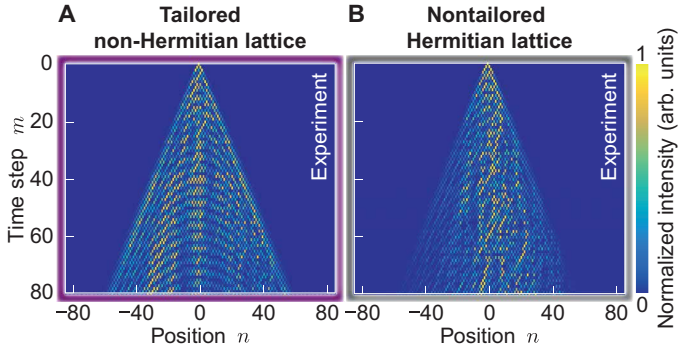

Fig. 4. Photonic realization of non-Hermitian–induced transparency. The experimental propagation data in the tailored lattice are compared to a general inhomogeneous lattice, upon a single-site excitation, i.e., a highly localized beam at $m = 0$. (**A**) When the real and imaginary part of the complex refractive index is tailored to fulfill the solution Eq. 7, the discrete diffraction pattern of a homogeneous lattice develops. In accordance to the solution (Eq. 7), such non-Hermitian transparency is induced only for a specific excitation. For deviating excitations, the lattice will be strongly opaque as shown in (**B**), where the lattice is not suitably tailored (see section S7). Remaining deviations can be explained by the experimentally limited accuracy. As before, the intensities in the shorter loop (called *u*) are depicted and normalized to the maximum of each time step. Note that the modulation of the complex potential now varies in time (or propagation direction). The full modulation patterns are presented in detail in section S6.

between experiment and simulation for induced transparency" section in Materials and Methods. The high similarity of strong interference contrasts in Fig. 4A to the unperturbed setting in Fig. 2B indicates many correct phase relations that have been achieved. Furthermore, we numerically verified that when we perfectly match the parameters in Eq. 7, the light follows the ideal discrete diffraction pattern (see section S6).

DISCUSSION

We have experimentally demonstrated non-Hermitian tailoring of an inhomogeneous optical mesh lattice in a photonic system. This non-Hermitian engineering can either be static, to realize shape-preserving beam transmission, or dynamic, to implement non-Hermitian–induced transparency. We anticipate our results to provide diverse routes for controlling the flow of light based on non-Hermitian photonics. In particular, the tailoring of the discrete lattice is precisely adjusted to the specific characteristics of the input excitation beam. This opens the way to designs where the transmission properties of the tailored medium are highly selective and thus may find application in secure data channeling.

MATERIALS AND METHODS

Implementation of a 1 + 1D time bin–encoded optical mesh lattice

The main principle of the creation of a photonic lattice by coupled fiber loops is similar to (*9*, *39*, *45*). Reduced to a minimum of components, this simplified setup consists of two loops of optical fiber and a beam splitter, which couples both loops. As the fiber loops differ in length, light propagating through that system has a different round trip time for each loop, $T + \Delta T$ for the longer loop and $T - \Delta T$ for the shorter one ($T > \Delta T$). If a short light pulse $t < \Delta T$ is inserted into this setup, then the evolution is the same as the propagation in a beam splitter pyramid (see fig. S1), which is a discrete-time quantum walk. Thus, the pulse dynamics can be mapped onto a 1 + 1D lattice. Thereby, every lattice site (m, n) encodes the arrival time $m \cdot T + n \cdot \Delta T$ of the corresponding pulse at the beam splitter. The number of whole round-trip times corresponds to the time step m, and the position n indicates which combination of long and short loop has been passed. A step to the right (green path) or left (yellow path) corresponds to a round trip through the longer or shorter loop, respectively. Pulses at the same lattice sites interfere, as they arrive the beam splitter at the same time. In this vein, the accumulated phase during the propagation through the loops does not have an influence because interfering pulses had propagated through a permutation of long/short loop, which means that the relative phase is not affected. In the same manner, every component added in the loops, for example, for phase or intensity modulation, is passed in every round trip, and thus, an exact copy of this component can be added to every lattice site in the lattice.

Detailed experimental setup and parameter value ranges

The main principle of this setup has been explained in the previous section. The setup that we will describe in the following resembles the setup of earlier work with a coupled fiber loops; see, for example, (*8*, *42*).

The setup is composed of two optical fiber loops, which are connected by a beam splitter with variable splitting ratio (Agiltron NanoSpeed) and thus creates a changeable coupling in the corresponding photonic lattice. In each loop, there is an acousto-optic modulator (AOM) (Brimrose Corp.) for the modulation of the amplitudes of the pulses (via the parameters G and F in Eq. 1) and a PM (iXblue Photonics) for modulating their phases (via the parameters φ and ψ in Eq. 1). The light is inserted into the loops by fiber couplers, which also couple part of the light out to reach photodetectors (Thorlabs). To be able to emulate gain and loss, the operating point of the AOMs is set to 50% of their maximal attenuation. An erbium-doped fiber amplifier (Thorlabs) in each loop compensates this suppression and other losses occurring during a round trip, for example, due to coupling light out for detection. In the following, a variation of the suppression level of the AOMs then can result in both gain and loss. The possible modulation parameters lie in the following ranges: $G^2 \in [0.49, 2.05]$; $F^2 \in [0.68, 1.46]$. Wavelength division multiplexers (AC Photonics) couple a distributed feedback (DFB) laser (JDS Uniphase) at a wavelength of 1538 nm to the amplifiers for optical gain clamping. This light is then removed from the system by a band-pass filter (WL Photonics). In addition, optical isolators (AC Photonics) take care of a unidirectional propagation and make sure that possible back reflections are suppressed.

The round-trip time is extended to roughly 24 μs by spools of optical single-mode fiber (SMF) (Corning Vascade LEAF EP). The difference between the loops of approximately 100 ns is inserted by an additional section of SMF (we used a standard SMF of SMF28 or comparable). Moreover, all fiber components are designed for a wavelength of 1550 nm. Some components operate in a polarization-dependent fashion (as, e.g., the PMs), mechanical polarization controllers are used for the alignment as indicated by three circles in fig. S2.

The signal that is inserted into the setup for excitation is a rectangular pulse of 60 ns. For this purpose, the continuous wave signal of the 1550 nm DFB laser (JDS Uniphase) is cut by a Mach-Zehnder

intensity modulator (SDL Integrated Optics Limited) to a rectangular pulse shape. An additional AOM is used here to further enhance the ratio between pulse plateau and ground level by lowering the latter and transmitting the pulse signal. All signals for the control of electro-optical devices are produced by arbitrary waveform generators (Keysight Technologies, 33622A).

An oscilloscope (Rohde & Schwarz, RTE1000) samples the detected and logarithmically amplified signal (logarithmic voltage amplifier) (Femto) in the loops after each round trip. The signal processing was performed in MATLAB, where the arrival times at the detector are translated into the according lattice sites with time step m and position n and matched the corresponding pulse height to get the propagation in the photonic lattice.

Calculation of the deviations between experiment and simulation for induced transparency

To support the visual comparison of the induced transparency images to the corresponding Hermitian ones, the difference between the experimental realizations (see Fig. 4, A and B) and the simulation of the ideal unscattered Hermitian case (see Fig. 2B) is calculated. To this end, the SSD is used with the normalization defined in Eq. 8. Before the calculation of the SSD, the data are prepared in two steps. First, the area $|n| > m$ is discarded, as this region cannot be reached by the spreading light pulses after a single-site excitation due to the discrete evolution protocol. Containing exclusively noise, it does, therefore, not carry any information about the performance of the setting. Second, the data are subsequently normalized to the sum of each time step. The normalization to the maximum of each time step (as has been done in Fig. 4) is beneficial for displaying the propagation but less suitable for quantitative calculations as broad intensity distributions would be weighed substantially higher than narrow ones. The prepared matrices are displayed in fig. S9 (A to C).

The SSD without normalization is a simple and commonly used method for image comparison and template matching (*46*–*48*), but also normalized variations have been used (*49*–*52*). For our specific purpose, we have used the L^2-norm of both compared matrices, which takes into account that the matrices are not necessarily Hermitian, and a scaling factor of $^1/_2$ so that the SSD lies in the range between 0 (signifying a perfect match) and 1 (denoting the worst case of entirely nonoverlapping matrices). In our case, the latter would, e.g., occur for two uniform distributions (prepared according to the steps above) residing on different sublattices (see fig. S9, F and G). For further benchmarks within this range, we have calculated the normalized SSD for random matrices of the same size (prepared according to the steps above) compared with the simulation and averaged over 1000 different realizations. For the random distributions without further restrictions, we find a value of 0.505, and 0.313 for distributions solely on the same sublattice as the simulation [see fig. S9 (D and E) for examples of the random matrices].

SUPPLEMENTARY MATERIALS

Supplementary material for this article is available at https://science.org/doi/10.1126/sciadv.abl7412

REFERENCES AND NOTES

1. J. B. Pendry, D. Schurig, D. R. Smith, Controlling electromagnetic fields. *Science* **312**, 1780–1782 (2006).
2. W. Cai, U. K. Chettiar, A. V. Kildishev, V. M. Shalaev, Optical cloaking with metamaterials. *Nat. Photon.* **1**, 224–227 (2007).
3. V. M. Shalaev, Optical negative-index metamaterials. *Nat. Photon.* **1**, 41–48 (2007).
4. K. G. Makris, R. El-Ganainy, D. N. Christodoulides, Z. H. Musslimani, Beam dynamics in PT symmetric optical lattices. *Phys. Rev. Lett.* **100**, 103904 (2008).
5. M. A. Miri, A. Regensburger, U. Peschel, D. N. Christodoulides, Optical mesh lattices with PT symmetry. *Phys. Rev. A* **86**, 023807 (2012).
6. S. Klaiman, U. Günther, N. Moiseyev, Visualization of branch points in PT-symmetric waveguides. *Phys. Rev. Lett.* **101**, 080402 (2008).
7. L. Feng, X. Zhu, S. Yang, H. Zhu, P. Zhang, X. Yin, Y. Wang, X. Zhang, Demonstration of a large-scale optical exceptional point structure. *Opt. Express* **22**, 1760–1767 (2014).
8. M. Wimmer, A. Regensburger, M. A. Miri, C. Bersch, D. N. Christodoulides, U. Peschel, Observation of optical solitons in PT-symmetric lattices. *Nat. Commun.* **6**, 7782 (2015).
9. A. Regensburger, C. Bersch, M. A. Miri, G. Onishchukov, D. N. Christodoulides, U. Peschel, Parity-time synthetic photonic lattices. *Nature* **488**, 167–171 (2012).
10. A. Guo, G. J. Salamo, D. Duchesne, R. Morandotti, M. Volatier-Ravat, V. Aimez, G. A. Siviloglou, D. N. Christodoulides, Observation of PT-symmetry breaking in complex optical potentials. *Phys. Rev. Lett.* **103**, 093902 (2009).
11. Y. D. Chong, L. Ge, H. Cao, A. D. Stone, Coherent perfect absorbers: Time-reversed lasers. *Phys. Rev. Lett.* **105**, 053901 (2010).
12. Y. Sun, W. Tan, H. Q. Li, J. Li, H. Chen, Experimental demonstration of a coherent perfect absorber with pt phase transition. *Phys. Rev. Lett.* **112**, 143903 (2014).
13. S. Longhi, PT-symmetric laser absorber. *Phys. Rev. A* **82**, 031801 (2010).
14. W. Wan, Y. Chong, L. Ge, H. Noh, A. D. Stone, H. Cao, Time-reversed lasing and interferometric control of absorption. *Science* **331**, 889–892 (2011).
15. K. Pichler, M. Kühmayer, J. Böhm, A. Brandstötter, P. Ambichl, U. Kuhl, S. Rotter, Random anti-lasing through coherent perfect absorption in a disordered medium. *Nature* **567**, 351–355 (2019).
16. B. Peng, Ş. K. Özdemir, S. Rotter, H. Yilmaz, M. Liertzer, F. Monifi, C. M. Bender, F. Nori, L. Yang, Loss-induced suppression and revival of lasing. *Science* **346**, 328–332 (2014).
17. M. Liertzer, L. Ge, A. Cerjan, A. D. Stone, H. E. Türeci, S. Rotter, Pump-induced exceptional points in lasers. *Phys. Rev. Lett.* **108**, 173901 (2012).
18. B. Bahari, A. Ndao, F. Valini, A. El Amili, Y. Fainman, B. Kante, Nonreciprocal lasing in topological cavities of arbitrary geometries. *Science* **358**, 636–640 (2017).
19. L. Pilozzi, C. Conti, Topological lasing in resonant photonic structures. *Phys. Rev. B.* **93**, 195317 (2016).
20. Z. Lin, H. Ramezani, T. Eichelkraut, T. Kottos, H. Cao, D. N. Christodoulides, Unidirectional invisibility induced by PT-symmetric periodic structures. *Phys. Rev. Lett.* **106**, 213901 (2011).
21. L. Feng, Y. L. Xu, W. S. Fegadolli, M. H. Lu, J. E. B. Oliveira, V. R. Almeida, Y. F. Chen, A. Scherer, Experimental demonstration of a unidirectional reflectionless parity-time metamaterial at optical frequencies. *Nat. Mater.* **12**, 108–113 (2013).
22. S. Longhi, Bidirectional invisibility in Kramers–Kronig optical media. *Opt. Lett.* **41**, 3727–3730 (2016).
23. T. T. Koutserimpas, A. Alù, R. Fleury, Parametric amplification and bidirectional invisibility in PT-symmetric time-Floquet systems. *Phys. Rev. A* **97**, 013839 (2018).
24. F. Loran, A. Mostafazadeh, Perfect broadband invisibility in isotropic media with gain and loss. *Opt. Lett.* **42**, 5250–5253 (2017).
25. S. A. R. Horsley, M. Artoni, G. C. La Rocca, Spatial Kramers-Kronig relations and the reflection of waves. *Nat. Photon.* **9**, 436–439 (2015).
26. V. V. Konotop, D. A. Zezyulin, Families of stationary modes in complex potentials. *Opt. Lett.* **39**, 5535–5538 (2014).
27. X. Zhu, L. Feng, P. Zhang, X. Yin, X. Zhang, One-way invisible cloak using parity-time symmetric transformation optics. *Opt. Lett.* **38**, 2821–2824 (2013).
28. K. G. Makris, Z. H. Musslimani, D. N. Christodoulides, S. Rotter, Constant-intensity waves and their modulation instability in non-Hermitian potentials. *Nat. Commun.* **6**, 7257 (2015).
29. K. G. Makris, A. Brandstötter, P. Ambichl, Z. H. Musslimani, S. Rotter, Wave propagation through disordered media without backscattering and intensity variations. *Light Sci. Appl.* **6**, e17035 (2017).
30. P. Sebbah, Scattering media: A channel of perfect transmission. *Nat. Photon.* **11**, 337–339 (2017).
31. K. G. Makris, Z. H. Musslimani, D. N. Christodoulides, S. Rotter, Constant intensity supermodes in non-Hermitian lattices. *IEEE J. Sel. Top. Quantum Electron.* **22**, 42–47 (2016).
32. A. F. Tzortzakakis, K. G. Makris, S. Rotter, E. N. Economou, Shape-preserving beam transmission through non-Hermitian disordered lattices. *Phys. Rev. A* **102**, 033504 (2020).
33. A. Brandstötter, K. G. Makris, S. Rotter, Scattering-free pulse propagation through invisible non-Hermitian media. *Phys. Rev. B.* **99**, 115402 (2019).
34. K. G. Makris, I. Krešić, A. Brandstötter, S. Rotter, Scattering-free channels of invisibility across non-Hermitian media. *Optica* **7**, 619–623 (2020).
35. I. Komis, S. Sardelis, Z. H. Musslimani, K. G. Makris, Equal-intensity waves in non-Hermitian media. *Phys. Rev. E.* **102**, 032203 (2020).

36. S. Yu, X. Piao, N. Park, Bohmian photonics for independent control of the phase and amplitude of waves. *Phys. Rev. Lett.* **120**, 193902 (2018).
37. S. A. R. Horsley, Indifferent electromagnetic modes: Bound states and topology. *Phys. Rev. A* **100**, 053819 (2019).
38. E. Rivet, A. Brandstötter, K. G. Makris, H. Lissek, S. Rotter, R. Fleury, Constant-pressure sound waves in non-Hermitian disordered media. *Nat. Phys.* **14**, 942–947 (2018).
39. A. Schreiber, K. N. Cassemiro, V. Potoček, A. Gábris, P. J. Mosley, E. Andersson, I. Jex, C. Silberhorn, Photons walking the line: A quantum walk with adjustable coin operations. *Phys. Rev. Lett.* **104**, 050502 (2010).
40. M. Wimmer, M. A. Miri, D. Christodoulides, U. Peschel, Observation of Bloch oscillations in complex PT-symmetric photonic lattices. *Sci. Rep.* **5**, 17760 (2015).
41. A. L. M. Muniz, M. Wimmer, A. Bisianov, U. Peschel, R. Morandotti, P. S. Jung, D. N. Christodoulides, 2D Solitons in in PT-Symmetric photonic lattices. *Phys. Rev. Lett.* **123**, 253903 (2019).
42. S. Weidemann, M. Kremer, T. Helbig, T. Hofmann, A. Stegmaier, M. Greiter, R. Thomale, A. Szameit, Topological funneling of light. *Science* **368**, 311–314 (2020).
43. A. Bisianov, M. Wimmer, U. Peschel, O. A. Egorov, Stability of topologically protected edge states in nonlinear fiber loops. *Phys. Rev. A* **100**, 063830 (2019).
44. E. J. Heller, R. Fleischmann, T. Kramer, Branched flow. *Phys. Today.* **74**, 44–51 (2021).
45. M. Wimmer, H. M. Price, I. Carusotto, U. Peschel, Experimental measurement of the Berry curvature from anomalous transport. *Nat. Phys.* **13**, 545–550 (2017).
46. S. Oron, T. Dekel, T. Xue, W. T. Freeman, S. Avidan, Best-buddies similarity - robust template matching using mutual nearest neighbors. *IEEE Trans. Pattern Anal. Mach. Intell.* **40**, 1799–1813 (2018).
47. A. Giachetti, Matching techniques to compute image motion. *Image Vis. Comput.* **18**, 247–260 (2000).
48. M. B. Hisham, S. N. Yaakob, R. A. A. Raof, A. B. A. Nazren, N. M. W. Embedded, Template matching using sum of squared difference and normalized cross correlation. *2015 IEEE Student Conf. Res. Dev. SCOReD 2015* , 100–104 (2015).
49. B. Pan, H. Xie, Z. Wang, Equivalence of digital image correlation criteria for pattern matching. *Appl. Optics* **49**, 5501–5509 (2010).
50. B. Pan, K. Li, W. Tong, Fast, robust and accurate digital image correlation calculation without redundant computations. *Exp. Mech.* **53**, 1277–1289 (2013).
51. B. Pan, K. Qian, H. Xie, A. Asundi, Two-dimensional digital image correlation for in-plane displacement and strain measurement: A review. *Meas. Sci. Technol.* **20**, 062001 (2009).
52. G. Facciolo, N. Limare, E. Meinhardt-Llopis, Integral images for block matching. *Image Process. Line.* **4**, 344–369 (2014).
53. T. Eichelkraut, R. Heilmann, S. Weimann, S. Stützer, F. Dreisow, D. N. Christodoulides, S. Nolte, A. Szameit, Mobility transition from ballistic to diffusive transport in non-Hermitian lattices. *Nat. Commun.* **4**, 2533 (2013).
54. M. Wimmer, A. Regensburger, C. Bersch, M. A. Miri, S. Batz, G. Onishchukov, D. N. Christodoulides, U. Peschel, Optical diametric drive acceleration through action-reaction symmetry breaking. *Nat. Phys.* **9**, 780–784 (2013).

Acknowledgments

Funding: A.Sz. thanks the Deutsche Forschungsgemeinschaft for funding this research (grants BL 574/13-1, SZ 276/9-2, SZ 276/15-1, and SZ 276/20-1) and the Krupp von Bohlen and Halbach foundation. The work of I.K. was funded by the Austrian Science Fund (FWF) Lise Meitner Postdoctoral Fellowship M3011 and the FWF grant P32300. The joint work of I.K., K.G.M., and S.R. was supported by the European Commission grant MSCA- RISE 691209. The computational results presented here have been obtained using the Vienna Scientific Cluster (VSC). **Author contributions:** All authors developed the concept. I.K. developed the theoretical framework for the non-Hermitian tailoring and provided simulation data. A.St., S.W., I.K., and M.K. designed the experimental implementation. A.St. performed the experiments in coupled fiber loops. A.St., S.W., M.K., M.H., and A.Sz. interpreted the experimental data. S.R. and A.Sz. supervised the project. All authors discussed the results and cowrote the paper. **Competing interests:** The authors declare that they have no competing interests. **Data and materials availability:** All experimental data and any related experimental background information not mentioned in the text can be found at the Rostock University Publication Server repository: https://doi.org/10.18453/rosdok_id00003418.

Submitted 2 August 2021
Accepted 7 April 2022
Published 25 May 2022
10.1126/sciadv.abl7412